Hindawi
International Journal of Polymer Science
Volume 2022, Article ID 8286518, 15 pages
https://doi.org/10.1155/2022/8286518

Research Article

Tunable Thin Film Periodicities by Controlling the Orientation of Cylindrical Domains in Side Chain Liquid Crystalline Block Copolymers

Lei Dong,[1] **Alvin Chandra**,[2] **Kevin Wylie**,[2] **Yuta Nabae**,[2] **and Teruaki Hayakawa**[2]

[1]*School of Materials Science and Engineering, Southeast University, Nanjing 211189, China*
[2]*Department of Materials Science and Engineering, School of Materials and Chemical Technology, Tokyo Institute of Technology, Ookayama, Meguro-ku, Tokyo 152-8552, Japan*

Correspondence should be addressed to Lei Dong; leidong@seu.edu.cn

Received 11 June 2022; Accepted 12 August 2022; Published 9 September 2022

Academic Editor: Mehdi Salami-Kalajahi

A facile approach to block copolymer (BCP) domain orientation control in thin films has been demonstrated by employing a BCP with liquid crystalline semifluorinated side chains by tuning the composition of the copolymers of the bottom surface layer (BSL). 1H,1H,2H,2H-Perfluorodecanethiol was attached to a precursor polymer, polystyrene-*block*-poly(glycidyl methacrylate) (PS-*b*-PGMA), to obtain a novel BCP with a C_8F_{17}-containing liquid crystal (LC) side chain (PS-*b*-P8FMA). Anisotropic hexagonally packed cylinder domains in a bulk state were first characterized by transmission electron microscopy (TEM) and small angle X-ray scattering (SAXS). The observed morphology transition of BCPs with different fluorinated side chain lengths of $-CF_3$, $-C_4F_9$, and $-C_6F_{13}$ suggested the decisive effects of LC side chain ordering on the anisotropic nanostructures. In the thin film study, poly(methyl methacrylate-*random*-2,2,2-trifluoroethyl methacrylate-*random*-methacrylic acid) (PMMA-*ran*-PTFEMA-*ran*-PMAA) solution was used as BSLs for tuning the desired periodicities. The surface free energy (SFE) of BSL was simply tailored by changing the composition of comonomers. In atomic force microscopy (AFM) characterization, long-range ordered perpendicularly oriented BCP domains in a hexagonally packed array or parallel oriented BCP domains as striation patterns were easily fabricated on non-preferential or preferential BSL, respectively. The study presents a novel approach to tunable thin film periodicities without changing or modifying BCPs, which is desired in next-generation BCP lithography.

1. Introduction

Block copolymers (BCPs) are widely studied due to their capability of self-assembling into a variety of long-ranged structure. The commonly observed morphologies in coil–coil flexible diblock copolymers include sphere, cylinder, gyroid, and lamellae, depending on the specific volume fraction of blocks [1–5]. This unique feature resulting from self-assembly behaviors reveals potential applications in perspective nanofabrication in the semi-conductor industry [6, 7]. However, compared to the conventional photolithographic technology, lithographic applications based on block copolymer self-assembly are confronted with the limitation on pattern type in the thin film. Therefore, BCPs of tunable thin film periodicities are in high demand.

The thin film periodicities could be tailored by BCPs of specific chain architectures with cross-linking technique [8] or using cyclic analogues instead of linear one [9]. Compared to alternating the chemical structure of BCPs, tuning thin film periodicities via precise control on thin film domain orientation is more appealing, as top and side views of the cylindrical domain indicate two accessible pattern types in thin films. Currently, most relevant thin film studies are based on semiflexible–flexible BCPs or side chain liquid crystalline (SCLC) block copolymer, as patterns of narrow domains and long-range orders could be obtained.

The self-assembly in semiflexible–flexible BCPs or SCLC may lead to unique domain packing array, which are usually associated with the BCP domain interface of non-constant mean-curvature. For instance, the observation of rectangular-shaped

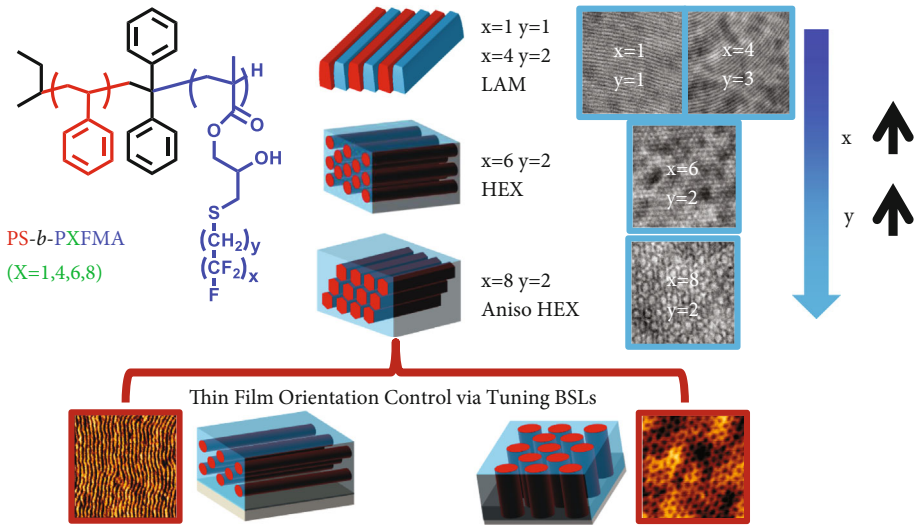

Scheme 1: Schematics of molecular design on BCPs and orientation control on thin film domain.

cylinder in rectangular array [10] and similar morphology predicted by self-consistent field theory (SCFT) [11] has been reported. Besides, the anisotropic packing of cylinder with stability in thermodynamics is predicted in rod-coil [12] or semiflexible–flexible BCPs [13, 14] using the SCFT model. The anisotropy in the self-assembly structure is also found in SCLC BCP, which is widely used for controlling the orientation of the BCP domains in thin films [15–18]. In the self-assembly process of SCLC BCPs, their microstructure will be influenced by two driving forces, side chain crystalline LC ordering and block segregation, which is different from self-assembly of coil–coil BCPs in which only block segregation will be involved. The periodicities of distinctive scales from side chain LC ordering and main-chain segregation of the counter-blocks will be co-existed and hence the hierarchical self-assembly will be governed by the combination of different driving forces [19]. Accordingly, modified models based on the SCFT approach [20] or dissipative particle dynamics (DPD) simulations [21–23] were developed to characterize the self-assembly behavior in SCLC or rod-coil BCP. Based on the experimental and theoretic studies, the hierarchical self-assembly system exhibits morphologies significantly different from those derived from conventional amorphous BCPs based on coil–coil model.

In previous studies, orientation tunings on BCP domain by introducing liquid crystal ordering [24–30] or other entropy-confined architecture [31] were widely reported for tailoring thin film pattern types. Verploegen et al. [32] manipulated the morphology of side chain liquid crystalline block copolymers through variations in the liquid crystalline content. Xie et al. [33] achieved the orientation control of BCP cylindrical domains by varying the substitution on the tail of the side chain azobenzene mesogen. Without chemical change in BCPs, Komura et al. [34] and Fukuhara et al. [35] developed a surface covering method to switch the parallel cylinder formation of BCP with liquid crystalline side chain to perpendicular cylinder formation or inversely. Wang et al. [36] developed a light-directed regulation of nanostructures in thin films of liquid crystalline diblock copolymers containing photoresponsive mesogen. Besides SCLC BCPs, Lo et al. [31] demonstrated that for star-block copolymers with symmetric volume fraction, perpendicularly oriented BCP nanostructures could be induced instead of enthalpy-driven parallel orientation via an entropic effect regulated by the number of arms. Isono et al. [37] utilized thermal annealing for inducing a drastic change in the domain orientation of a biomass-based A–B–A triblock copolymer from horizontal to vertical. However, these methodologies all involve the massive synthesis work or time-consuming process. Besides, the improvements on orders of thin film patterns were in demand.

In this study, the precise orientation control on thin film BCP domain is readily realized by tuning the composition of bottom surface layer (BSL) copolymers. Two thin film pattern types, striations and hexagonally packed dots, were thereby prepared. To further investigate the observed anisotropic packing array caused by LC side chain ordering, the effects of the fluorinated side chain length on the self-assembly morphologies were studied using BCPs of CF_3, C_4F_9, C_6F_{13}, and C_8F_{17}-containing side chains, as the side chain liquid crystalline properties are highly dependent on the lengths of introduced side chains. The molecular design on BCPs and orientation control on thin film domain are schematically demonstrated in Scheme 1.

2. Experimental Section

2.1. Materials. Lithium chloride (LiCl) obtained from Kanto Chemical Co. Inc. was baked at 200°C prior to use. Styrene was washed by 0.1 M sodium hydroxide (NaOH) aqueous solution for three times and dried by magnesium sulfide ($MgSO_4$); then, calcium hydride (CaH_2) was added and stirred overnight before distillation. After the distillation, di-*n*-*butyl*magnesium ($MgBu_2$) was added under Ar protection to remove the residual water in styrene. A secondary distillation was further carried out to degas using liquid nitrogen as

the freezing source. Similarly, glycidyl methacrylate (GMA) was distilled, dehydrated by CaH_2, and subsequently degassed under Ar. Diphenylethene (DPE) was distilled, dehydrated by *n*-butyl lithium, and subsequently degassed under Ar. 3,3,4,4,5,5,6,6,6-Nonafluoro-1-hexanethiol was synthesized from 1,1,1,2,2,3,3,4,4-nonafluoro-6-iodohexane, which was purchased from Sigma-Aldrich. The synthesis approach was carried out following the previous literature [38]. The ^{1}H NMR spectra of the prepared 3,3,4,4,5,5,6,6,6-nonafluoro-1-hexanethiol are presented in the Supporting Information (SI).

All other materials purchased from FUJIFILM Wako Pure Chemical Corporation, Tokyo Chemical Industry, and Sigma-Aldrich were of reagent grade and used as received. The synthesis routines of homopolymers with varied side chains and random copolymers are presented in the SI.

2.2. Methods. ^{1}H NMR spectra were performed on a JEOL JNM-ECS400 (400 MHz) instrument using chloroform-*d* as the solvent. SEC (size exclusion chromatography) analysis was carried out with a Shodex GPC-101 instrument, which was equipped with columns of Shodex LF804. The number-average molecular weights (M_n) and molecular weight distributions (M_w/M_n) were measured by SEC with polymer/tetrahydrofuran solution containing 0.01 mol/L of lithium bromide (LiBr) at a flow rate of 1.0 ml/min at 40°C and calibrated with polystyrene. Thermal behaviors of polymer were estimated from a Seiko DSC 7020 differential scanning calorimeter (DSC) at a scanning rate of 10°C/min under a nitrogen flow. The transition temperature values were determined from the second heating and cooling scan. The scanning temperature range was set from 25°C to 250°C, and the second scanning curve was used for analysis. Microscopic observation of thermal events was also conducted using an Olympus BH-2 polarized optical microscope equipped with a Mettler FP82HT hot-stage system. Small angle X-ray scattering (SAXS) measurements were performed on a Bruker SAXS NanoSTAR (output: 50 kV, 50 mA) instrument. After monochromatic processing by a Göbel mirror, a concentrated CuKα radiation (wavelength: 1.5416 Å) was applied to the sample. The scatted X-ray was collected by a 2D-PSPC detector to determine the morphologies in bulk sample. Synchrotron radiation was carried at Spring-8 out using beam line BL40B2 with a sample-to-detector of 2.0 meters. Wide-angle X-ray scattering (WAXS) measurements were carried out using a Bruker NanoSTAR-U instrument equipped with imaging plate (IP) at a distance of 210 mm from the sample using CuKα radiation (wavelength: 1.5416 Å). The WAXS pattern recorded on the IP was read and analyzed by a Rigaku automatic X-ray imaging system (R-AXIS) DS3C. Bright-field transmission electron microscopy (TEM) images of the sample structure were also obtained using a Hitachi H7650 Zero A under an 80 kV accelerating voltage. Bulk samples were prepared for TEM analysis by first being pasted onto epoxy resin for handling and then microtomed (Reichert-Jung Ultracut E) by a DiATOME diamond knife to a thickness of 70 nm. The sections produced were then placed onto TEM grids and stained by ruthenium oxide for observation. Steady shear alignments were performed on a UBM Rheosol-G3000 rheometer equipped with a cone-plate fixture with 25 mm in diameter at 200°C until the steady viscosity was observed (typical shearing period is 1.5 h). After stopping the shear flow, the BCP thick film sample with 400 μm thickness was cooled to 150°C and kept for 3 h. Then, the sample was cooled to room temperature and removed from the rheometer fixture by putting it into ethanol. The orientations of the LC mesogens and the microcylinders in the sheared sample were determined by SAXS patterns in various three characteristic vorticity ($v \times \nabla v$), velocity (v), and velocity gradient (∇v) directions. Contact-angle measurements were carried out using a Kyowa DM-501YH instrument. O_2-RIE treatments were performed by etching instrument (SATO VAC, Inc.). The oxygen flow rate was set to 40 sccm and the applied power used was 20 W. The thin film samples were fabricated using a spin coater MIKASA IH-D7, and the film thicknesses were determined by a FILMETRICS F20-EXR. To observe the surface morphology of BCP thin films, an atomic force microscope (AFM) (NanoWizard Ultra Speed A, JPK) was utilized.

2.3. Synthesis of PS-b-PGMA. The synthetic routine to targeted diblock copolymer was classified into two steps, the synthesis of precursor main-chain polymer PS-*b*-PGMA via sequential anionic living polymerization and the subsequent post-functionalization for introduction of fluorine-rich side chain.

The anionic polymerization of styrene and GMA is illustrated by the following example. All anionic polymerization procedures were performed under Ar protection. First, 30 mL of THF with LiCl (29.7 mg, 0.700 mmol) was added into a 50 mL Schlenk flask and then cooled to −78°C using a cooling bath. Excess amount of *sec*-Butyllithium (*sec*-BuLi) (in 1.05 M hexane/cyclohexane solution) was added until the solution color changed to yellow for the purification. Then, the Schlenk flask was removed from the cooling bath and kept under room temperature until the solution became colorless. The Schlenk flask was again cooled to −78°C, and a fixed amount of *sec*-BuLi solution (0.69 mL, 0.700 mmol) was added as initiator. Styrene (1.65 mL, 14.42 mmol) was further added and stirred for 30 min, resulting in bright orange color of the solution. DPE (0.39 mL, 2.1 mmol) was added, causing a change to deep red color. After 30 min of stirring, GMA (0.47 mL, 3.52 mmol) was added and stirred for another 30 min. The color of solution quickly disappeared. Finally, 3 mL of methanol (MeOH) (excess amount) purged with Ar was added to yield proton-terminated PS-*b*-PGMA. The polymer was precipitated into MeOH and collected by filtration. Then, the product was dried at 40°C under a reduced pressure to yield PS-*b*-PGMA as a white powder (1.80 g, 90% yield).

The M_n and dispersity ($Đ = M_w/M_n$) of the product determined by SEC were 3900 g mol^{-1} and 1.23, respectively.

^{1}H NMR (400 MHz, $CDCl_3$, δ, ppm): 0.98 (s, α-CH_3, PGMA), 1.14 (s, α-CH_3, PGMA), 1.29–1.80 (br, backbone, –CH_2–CH–, PS), 1.84–2.30 (br, backbone, –CH_2–CH–, PS, br, backbone, –CH_2–C(CH_3)–, PGMA), 2.70 (s, –CH_2–CH(CH_2)–O–, PGMA), 2.82 (s, –CH_2CH(CH_2)–O–, PGMA), 3.28 (s, –CH_2–CH(CH_2)–O–, PGMA), 3.84 (s, –(C=O)O–CH_2–,

PGMA), 4.37 (s, –(C=O)O–CH_2–, PGMA), 6.39–6.85 (*m*, *o*-aromatic, PS) 6.91–7.42 (*m*, *m*-, *p*-aromatic, PS).

2.4. Synthesis of PS-b-PXFMA (X = 1or 4 or 6 or 8) through the Post-Functionalization of PS-b-PGMA with 2,2,2-Trifluoroethanethiol or 3,3,4,4,5,5,6,6,6-Nonafluoro-1-hexanethiol or 3,3,4,4,5,5,6,6,7,7,8,8,8-Tridecafluoro-1-octanethiol or 1H,1H,2H,2H-Perfluorodecanethiol. Thiol-epoxy click reaction was utilized to introduce the semi-fluorinated side chains to the backbone of precursor copolymers PS-*b*-PGMA. The general procedure is as follows regardless of the type of thiols: a 10 ml glass tube was charged with PS-*b*-PGMA and THF (20 mole equiv. to PGMA repeating units) and immersed in an ice-water bath. 1 wt% lithium hydroxide (LiOH) aqueous solution (LiOH 0.05 mole equiv. to PGMA repeating units) and thiol (1.3~1.5 mole equiv. to PGMA repeating units) were added to the tube. After stirring for 20 min, the tube was transferred to a thermal reactor preset to 30°C and stirred for 3 h. The crude solution was precipitated in hexane or methanol or mixture of water and methanol, depending on the M_n of BCP and type of thiol. After filtration, the solid was again dissolved in THF and precipitated and then filtered two more times to remove any residual reagents. Eventually the product was dried at room temperature under a reduced pressure to yield a white powder (41% yield).

2.4.1. Characterization of PS-b-P1FMA. ^{1}H NMR (400 MHz, $CDCl_3$, δ, ppm): 0.95 (s, α-CH_3, P1FMA), 1.07 (s, α-CH_3, P1FMA), 1.22–1.70 (br, backbone, –CH_2–CH–, PS), 1.72–2.23 (br, backbone, –CH_2–CH–, PS, br, backbone, –CH_2–$C(CH_3)$–, P1FMA), 2.72–2.90 (*m*, –CH(OH)–CH_2–S–, P1FMA), 3.11–3.31 (q, –S–CH_2–CF_3, P1FMA), 3.88–4.18 (m, –(C=O)O–CH_2–CH(OH)– P1FMA), 6.28–6.73 (*m*, *o*-aromatic, PS), 6.86-7.32 (*m*, *m*-, *p*-aromatic, PS).

2.4.2. Characterization of PS-b-P4FMA. ^{1}H NMR (400 MHz, $CDCl_3$, δ, ppm): 0.96 (s, α-CH_3, P4FMA), 1.12 (s, α-CH_3, P4FMA), 1.20–1.68 (br, backbone, –CH_2–CH–, PS), 1.70–2.28 (br, backbone, –CH_2–CH–, PS, br, backbone, –CH_2–$C(CH_3)$–, P4FMA), 2.30–2.50 (t, –CH_2–CF_2–, P4FMA), 2.60–2.76 (t, –S–CH_2–CH_2–CF_2–, P4FMA), 2.76–2.87 (d, –CH(OH)–CH_2–S–, P4FMA), 3.82–4.17 (d, –(C=O)O–CH_2–, P4FMA) (*m*, –CH(OH)–, P4FMA), 6.28–6.85 (*m*, *o*-aromatic, PS), 6.86–7.32 (*m*, *m*-, *p*-aromatic, PS).

2.4.3. Characterization of PS-b-P6FMA. ^{1}H NMR (400 MHz, $CDCl_3$, δ, ppm): 0.98 (s, α-CH_3, P6FMA), 1.12 (s, α-CH_3, P6FMA), 1.21–1.70 (br, backbone, –CH_2–CH–, PS), 1.72–2.25 (br, backbone, –CH_2–CH–, PS, br, backbone, –CH_2–$C(CH_3)$–, P6FMA), 2.29–2.50 (t, –CH_2–CF_2–, P6FMA), 2.60–2.76 (t, –S–CH_2–CH_2–CF_2–, P6FMA), 2.76–2.87 (d, –CH(OH)–CH_2–S–, P6FMA), 3.82–4.17 (d, –(C=O)O–CH_2–, P6FMA) (*m*, –CH(OH)–, P6FMA), 6.28–6.85 (*m*, *o*-aromatic, PS), 6.86–7.32 (*m*, *m*-, *p*-aromatic, PS).

2.4.4. Characterization of PS-b-P8FMA. ^{1}H NMR (400 MHz, $CDCl_3$, δ, ppm): 0.98 (s, α-CH_3, P8FMA), 1.12 (s, α-CH_3, P8FMA), 1.21–1.70 (br, backbone, –CH_2–CH–, PS), 1.72–2.25 (br, backbone, –CH_2–CH–, PS, br, backbone, –CH_2–$C(CH_3)$–, P8FMA), 2.29–2.50 (t, –CH_2–CF_2–, P8FMA), 2.60–2.76 (t, –S–CH_2–CH_2–CF_2–, P8FMA), 2.76–2.87 (d, –CH(OH)–CH_2–S–, P8FMA), 3.82–4.17 (d, –(C=O)O–CH_2–, P8FMA) (*m*, –CH(OH)–, P8FMA), 6.28–6.85 (*m*, *o*-aromatic, PS), 6.86–7.32 (*m*, *m*-, *p*-aromatic, PS).

2.5. Bulk Sample Preparation. The bulk samples for the investigation on bulk morphologies and domain spacings (*d*-spacing) of the self-assembled nanostructures were prepared by slowly evaporating a dilute BCP THF solution filtered through a 0.25 μm pore size PTFE membrane syringe filter at 30°C. The as-prepared samples were further annealed at 150°C for 24 h under a reduced pressure.

2.6. Thin Film Preparation. Bare silicon wafers cut into 1 cm^2 pieces were washed in toluene for 3 min with sonification, and dried in streams of nitrogen. The washed wafers were then treated with a mixture of H_2O_2 (30%) and H_2SO_4 (70%) (v/v) at 80°C for 40 min. Then, the wafers were rinsed with water repeatedly and dried. BSL was generated by spin coating a 1.0 wt% poly(2, 2, 2-trifluoroethyl methacrylate)-*random*-poly(methyl methacrylate)-*random*-poly(methacrylic acid) (PTFEMA-*r*-PMMA-*r*-PMAA) solution in propylene glycol monomethyl ether acetate (PGMEA) solution at 3000 rpm for 30 s onto the cleaned silicon wafers, followed by cross-linking at 200°C for 5 min. The silicon substrates were subsequently sonicated in toluene to remove any unattached random copolymers and rinsed with fresh toluene. Furthermore, approximately 1.0 wt % solutions of the BCPs in toluene were spin-coated at 3000 rpm for 30 s onto the surface-modified silicon substrates to obtain thin films with ca. 1.5 L_0 thicknesses (1.0 L_0 denotes one periodic length of self-assembled nanostructure). The as-prepared thin films were further annealed at 150°C for 24 h. An O_2-RIE treatment was carried out for a certain time (40 sccm, 20 W, 20 Pa) to selectively remove the methacrylate-based segments.

3. Results and Discussion

3.1. Synthesis and Characterization of the Homopolymers. The homopolymers with fluorinated side chains of various length were first synthesized using the same precursor homopolymer PGMA and corresponding characteristics were investigated. The precursor homopolymer PGMA was prepared via living anionic polymerization of GMA monomer using *sec*-BuLi as initiator in THF under –40°C. By control on the molar ratio of initiator to monomer, M_n of the synthesized PGMA was intentionally kept low because of the poor solubility of the post-functionalized homopolymers especially with the relatively long side chains. The broadening of the molecular weight dispersity of homo-PGMA ($\oplus$ = 1.18), as well as PS-*b*-PGMA ($\oplus$ = 1.23), are thought caused by the diffusional restriction of the monomer access towards the living centers [39], because of lesser solvation and increasing compactness of the polymer coils in low temperature THF solvent. In the thiol-epoxy reaction, PGMA was mixed with approximately 1.5 times of excessive thiols in THF solution loaded with catalytic amount of LiOH at 30°C. LiOH is considered as the optimized catalyst as quantitative

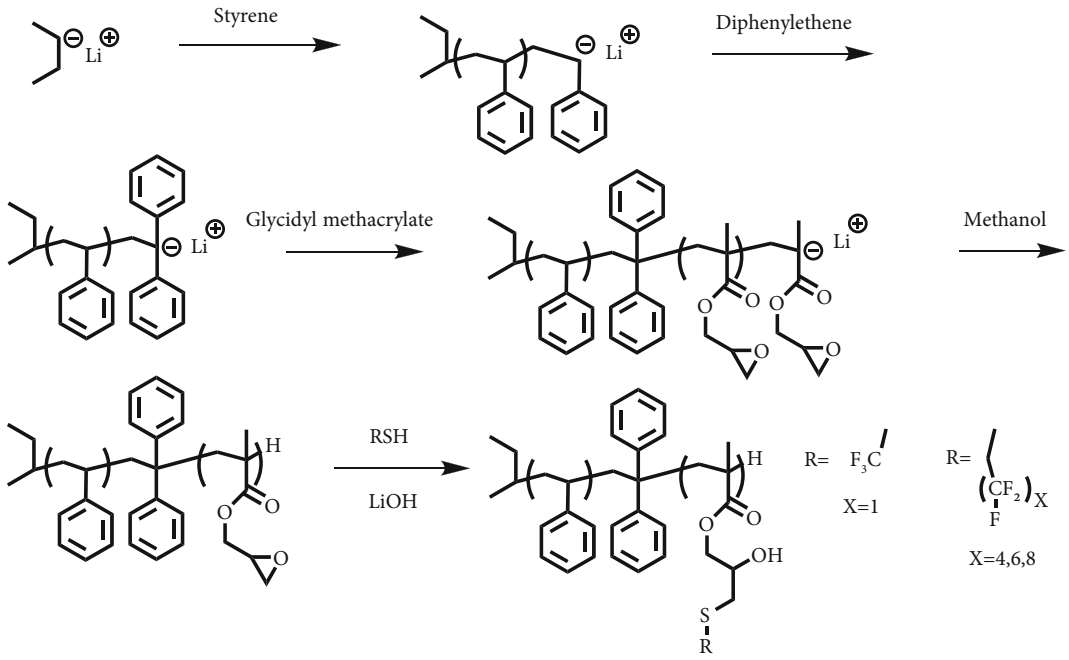

Scheme 2: Synthetic scheme of PS-*b*-PGMA precursor via sequential living anionic polymerization of styrene and glycidyl methacrylate and post-functionalization with a variety of semi-fluorinated thiols.

conversions are obtained at a catalyst loading over a few hours' reaction time under mild reaction temperatures.

The synthesized homopolymers, including homo-P4FMA, homo-P6FMA, and homo-P8FMA were characterized by NMR, SEC, DSC, and WAXD (Figures S1–S5, SI) and summarized (Table S1, SI). The properties of homo-P1FMA were listed in our previously published paper [40]. In NMR spectra, homo-P8FMA only reveals the characteristic proton signals from polymer backbone because of the bulky C_8F_{17} side chain of high rigidity. The solubility of homopolymer in THF or chloroform was significantly improved as the length of introduced side chain was reduced. Except C_8F_{17}-containing homopolymer, other homopolymers reveal the characteristic proton signals from various side chains and the epoxy unit in precursor PGMA becomes disappeared, indicating the nearly 100% introduction rate of side chain. In SEC results, a significant shift to higher M_n was observed after thiol-epoxy reaction and the measured M_n of homopolymers were in good agreement with the M_n estimated from precursor PGMA, indicating the complete conversion in chemical modification. Additionally, the thermal analysis reveals an increased T_g of homopolymer with elongated side chain, which is highly correlated with the reduced mobility of elongated semi-fluorinated side chain. More importantly, significant transitions from LC to isotropic phase were detected in C_6F_{13} and C_8F_{17}-containing homopolymers. In contrast, CF_3 and C_4F_9-containing homopolymers merely reveal a glass transition within the scanning temperature range. The liquid crystalline (LC) structures of C_6F_{13} and C_8F_{17}-containing homopolymers in bulk were further characterized by X-ray. The LC lamellar structure of 3.2 nm and 3.6 nm periodicity was observed in C_6F_{13} and C_8F_{17}-containing homopolymers, respectively. C_8F_{17}-containing homopolymer reveals a higher periodicity evidenced by more refined diffraction peaks. According to the previous study on the relationship between LC phase and number of fluorocarbons in side chain [41], smectic LC phase may be formed in C_6F_{13} and C_8F_{17}-containing homopolymer. The *S-cis* conformation of semi-fluorinated side chain was also reconstructed using MM2 energy-minimization based on Chem 3D 16.0 (Figure S6, SI). The estimated distance in the model compound from backbone carbon atom to end carbon atom of $-CF_3$ is 1.5 nm (C_6F_{13}-containing side chain) and 1.8 nm (C_8F_{17}-containing side chain), respectively, which are in good agreement with the half LC periodic length estimated from WAXD. Based on the molecular simulation results, a single LC periodic length is composed of a pair of mesogens with head-to-head stereo-regularity [42].

The surface free energies (SFEs) of PXFMA with various semi-fluorinated side chain length, estimated via the water and diiodomethane contact-angle measurements based on the Owens–Wendt method was 33.3 [40], 25.7, 23.1, and 21.6 mJ m^{-2}, respectively (Table S6). SFE of PS was measured to be 40.7 mJ m^{-2} [43]. Comparatively, the SFE of poly(2,2,2-trifluoroethyl methacrylate) (PTFEMA) was measured to be 25.1 mJ m^{-2} using the same method. For CF_3-containing side chain, the hydrophobicity of CF_3 and the hydrophilicity of hydroxyl group will be cancelled off with each other. Therefore, a balance between SFEs of PS and CF_3-containing P1FMA block was achieved for perpendicular orientation on BCP domain in thin film. However, the introduction of the elongated semi-fluorinated side chain contributed more to the hydrophobicity of PXFMA block and a gradually decreasing SFE value was accompanied.

Table 1: Characterization data of the synthesized BCPs.

BCP	Label[a]	M_n[b] (kg Mol^{-1})	$Đ$	w_{PS}[c]	f_{PS}[c]	$d_{spacing}$[d] (nm)	LC periodicity[e] (nm)	Morphology[f]
PS-*b*-PGMA	SG4	3.9	1.23	0.73	0.68	8.9	—	Disorder
PS-*b*-P1FMA	S1F	5.2	1.25	0.60	0.67	9.6	—	LAM
PS-*b*-P4FMA	S4F	6.4	1.21	0.48	0.56	12.1	(2.6)	LAM
PS-*b*-P6FMA	S6F	6.6	1.19	0.42	0.54	11.6	3.2	HEX
PS-*b*-P8FMA	S8F	7.5	1.18	0.38	0.50	11.5	3.6	Asym HEX

[a]The labels SG and S(X)F refer to PS-*b*-PGMA and PS-*b*-PXFMA, respectively, while the number to the right refers to the number-average molecular weight (M_n) of the polymer. [b]M_n and dispersities ($Đ$) were obtained by SEC using THF as the eluent based on PS standards. [c]PS weight fractions (w_{PS}) of PS-*b*-PGMA were calculated via ^{1}H NMR and PS weight (w_{PS}) and volume fractions (f_{PS}) of PS-*b*-PXFMA were further estimated based on 100% introduction rate of side chain using bulk densities for each block (1.05 g cm^{-3} for PS, 0.805 g cm^{-3} for PGMA, 1.43 g cm^{-3} for P1FMA, 1.45 g cm^{-3} for P4FMA, 1.66 g cm^{-3} for P6FMA and 1.73 g cm^{-3} for P8FMA). [d]The domain spacings (d-spacing) were estimated from the position of first-order scattering peak in the SAXS profile upon thermal annealing at 150°C for 24 h. [e]The periodicity of LC side chain was determined by the position of first-order scattering peak in the WAXD profile of homopolymer upon thermal annealing at 150°C for 24 h. [f]The bulk morphologies were determined by SAXS and TEM.

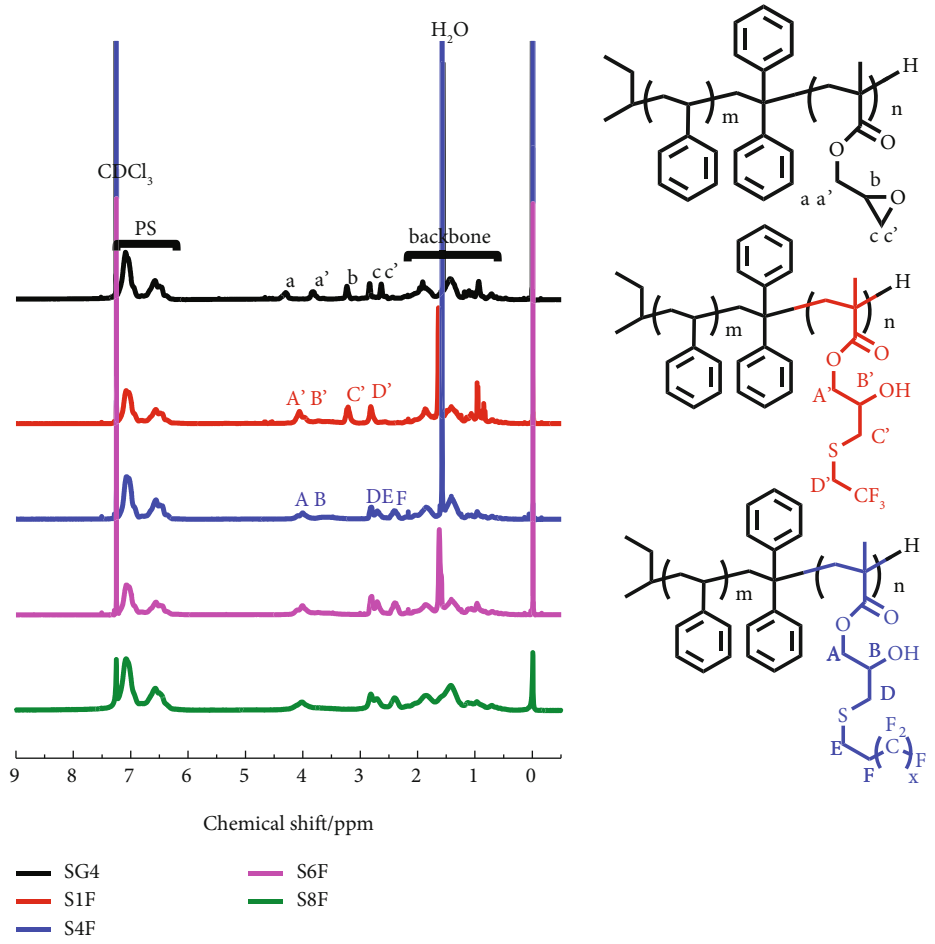

Figure 1: ^{1}H NMR spectra of PS-*b*-PGMA (SG4) and chemically modified PS-*b*-PXFMA (abbreviated as S1F, S4F, S6F, and S8F).

3.2. Synthesis and Characterization of the BCPs. PS-*b*-PGMA precursor polymer (SG4) was successfully synthesized via the sequential anionic polymerization (Scheme 2). Based on NMR and SEC analyses, the synthesized BCPs revealed a molecular weight of 3.9 kg mol^{-1} and a narrow dispersity of 1.23.

Semi-fluorinated thiols of various F numbers were then introduced to the precursor PS-*b*-PGMA in THF solution with LiOH as the catalyst at 30°C for 3 h reaction. The M_n of the BCPs were increased in accordance with the molecular weight of introduced thiol, while dispersities remained low (Table 1 and Figure S7, SI) Besides, the characteristic ^{1}H NMR signals corresponding to the glycidyl moieties in PS-*b*-PGMA (*a*, *a*′, *b*, *c*, and *c*′ at 2.70, 2.82, 3.28, 3.84, and 4.37 ppm, respectively) (Figure 1) had disappeared and the signals attributed to the introduced side chains were observed,

indicating the complete conversion of side chain functionalities in all chemical modifications.

In thermal analysis (Figure S8, SI), only S6F and S8F with sufficient long semi-fluorinated side chain reveal a transition from LC ordered phase to isotropic phase. Besides, T_g mainly attributed to PS segments almost remained constant because of the same PS-*b*-PGMA precursor polymer used in the study. The observation results of BCPs are in good agreement with those revealed in homopolymer studies.

3.3. Morphologies in the Bulk. The bulk morphologies of the synthesized PS-*b*-PXFMAs were then analyzed via SAXS (synchrotron radiation) and TEM characterizations (Figures 2–4).

The precursor PS-*b*-PGMA (SG4) exhbits a disordered morphology because of the relatively low χ parameter [40]. However, following the chemical modifcation of semi-fluorinated side chain, all PS-*b*-PXFMAs reveal significant self-assembly morphologies, indicating enhanced χ parameters. The $d_{spacing}$ estimated from the position of primary scattering peak in SAXS is narrowly distributed among 9.6–12.1 nm, which are reasonably attributed to the similar M_n and estimated χ_{eff} of PS-*b*-PXFMAs. However, the observed morpology of PS-*b*-PXFMAs exhibits a transition from lamellar to hexagonally packed cylinderical type as the incorporated side chain becomes longer. The SAXS profiles of amorphous PS-*b*-P1FMA and PS-*b*-P4FMA both suggest q ratios of integers, which are representative indicators of formation of lamellar morphology. A lamellar morpholgy of PS-*b*-P1FMA with similar M_n and more symmetric volume fraction ($f_{ps} = 0.62$) was also observed in the reported experimentals [40]. Besides, an insignfcant 2.6 nm periodic length was detected by SAXS, which is related to the extremly weak ordering from C_4F_9 side chain. Accordingly, no signifcant LC phase transition was observed in DSC analysis. The thresohold of side chain length for exhibiting significant LC phase is C_6F_{13}. Owing to the formation of side chain LC structure, a hierarchical self-assembly strucuture containing segments segregation and LC ordering begins to emerge. A lamellar structure of 3.2 nm periodic length was indicated by the X-ray analysis on PS-*b*-P6FMA and corresponding homopolymer. DSC results also suggested a transition from the assigned smectic to isotripic phase at 126°C, which is below the annealing temperature of 150°C. Therefore, the contribution from side chain LC ordering is partially suppressed during the thermal annealing process. The SAXS characterizaiton revealed characteristic q ratios of $1:\sqrt{3}:2$ in response to anisotropic hexagonally packed cylinderical morphology. The significant peak with q ratio of $\sqrt{3}$ indicates the high symmetry of hexagonal array. Besides, the isotropy of hexagonal array was also evidenced by the TEM observation results (Figure 3). The self-assembled cylinderical morphology from symmetic diblock copolymer with LC side was also predicted by SCFT theory [20].

Addtionally the SAXS profiles of amorphous PS-*b*-P1FMA, PS-*b*-P4FMA, and liquid crystalline PS-*b*-P6FMA were analyzed using Scatter (version 2.5, 03/2011) (Figure S9 in SI). The predicted periodic nano-strucutres estimated from the fitting profiles are highly consistent with the TEM

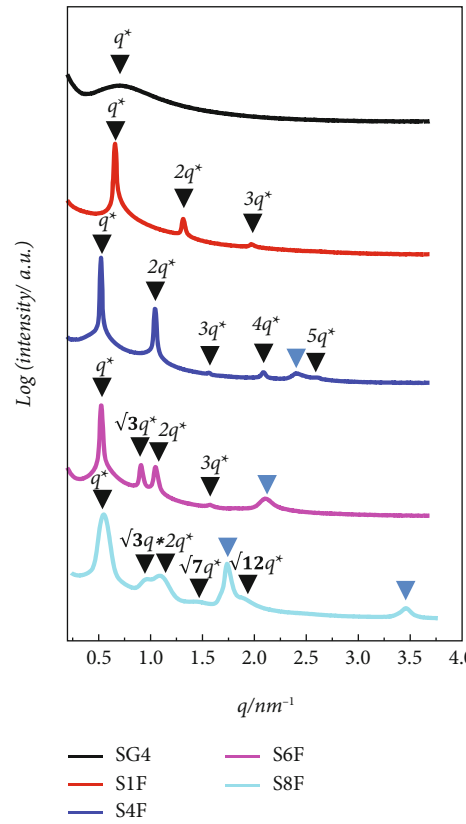

FIGURE 2: SAXS profiles of the precursor PS-*b*-PGMA and PS-*b*-PXFMAs ($X = 1, 4, 6,$ and 8) bulk samples following thermal annealing. The blue triangle indicates the peak from LC phase of side chain.

observations (Figure 3). PS-*b*-P4FMA reveals a more anisotropic lamellar structure in compasion with that of PS-*b*-P1FMA, which is possibly related to the weak ordering of fluorinated side chain. The minor domain of 4.1 nm width is possibly consisted of an adjacent pair of C_4F_9 side chain with a predicted 2.6 nm length. For PS-*b*-P6FMA with significant LC side chain ordering, hexagonally packed cylinders with 5.4 nm radius are predicted. The volume fraction of cylinder is estimated being 0.56, which is close to the estimated PS volume fraction ($f_{PS} = 0.54$) in synthesis characterizaiton. Beisdes, the minmial spacing between adjacent cylinders is esimtated being 3.0 nm, which is close to the spacing of a pair of C_6F_{13} side chain in head-to-head regularity. Therefore, the self-assembly morpholgy transition is likely caused by the spacing confinments from the enhanced side chain ordering.

As the length of side chain was further increased to C_8F_{17}, LC lamellar strucutre of higher periodicity and larger periodic legnth is expected based on the previous study [41]. The interpaly between the segments segregation and enhanced LC ordering creates a unique anisotropic morphology, which is different from any known morphology reuslting from amorphous BCP. First, SAXS reveal a significant primary scattering peak in response to 3.6 nm $d_{spacing}$ and its sceondary scattering peak at $2q$ position could be even detected, indicating a well-defined lamellar structutre.

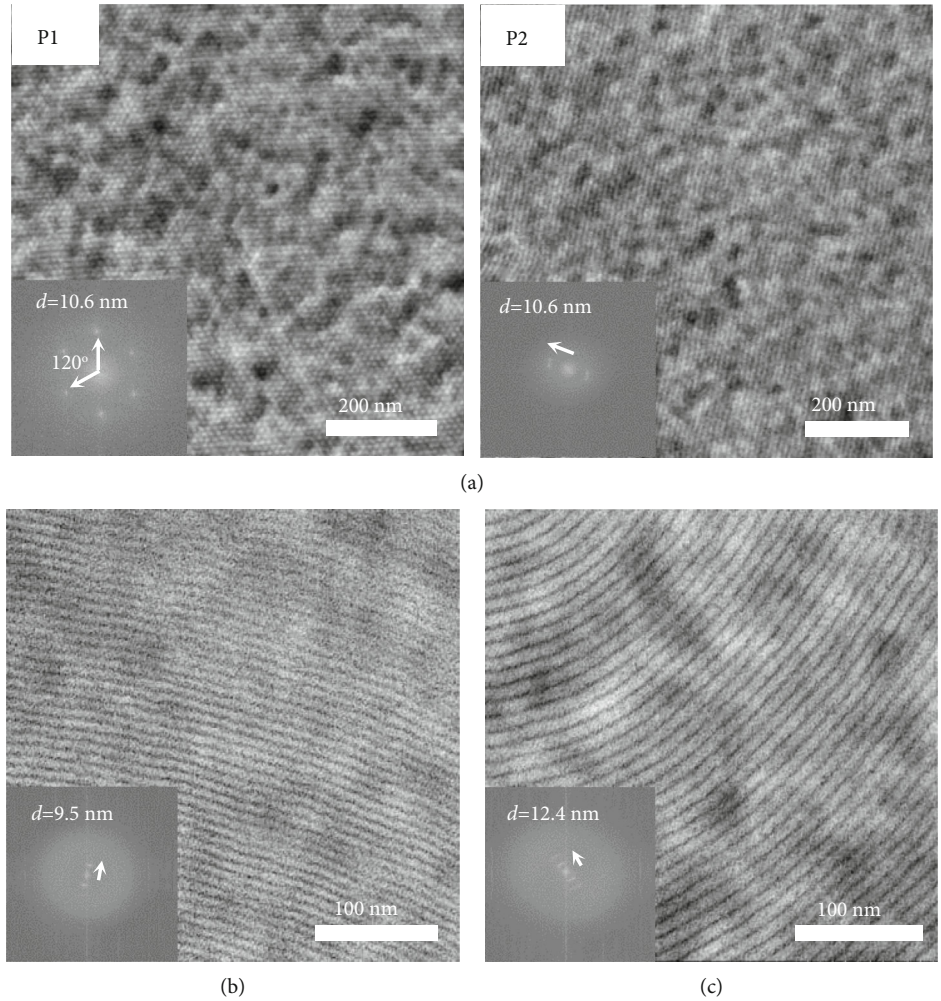

Figure 3: (a) TEM micrographs showing the regular symmetric hexagonally packed cylindrical morphology of annealed PS-*b*-P6FMA bulk sample. Two phases noted as P1 and P2 are from top and side view of the cylinder structure, respectively. The bottom left inset in TEM images displays the Fourier-transform pattern of the real-space image and in P1 six periodic lengths of 10.6 nm with an averaged 60 intersection angle indicating symmetric hexagonal packed array are clearly revealed. (b) TEM micrographs showing the averaged 9.5 nm width lamellar morphology of annealed PS-*b*-P1FMA bulk sample. (c) TEM micrographs showing the averaged 12.4 nm width lamellar morphology of annealed PS-*b*-P4FMA bulk sample. The bright and dark region corresponds to PS and heavily ruthenium tetroxide-stained hydroxyl groups in fluorinated segments, respectively.

This observation on BCPs were also highly consistent with the lamellar stucutre chararterized in correpoding homopolymer. Combined with the observed narrower transition peaks in DSC of both BCP and homopolymer compared to those of PS-*b*-P6FMA, a smectic phase with higher periodicity than that of PS-*b*-P6FMA could be assgined to LC ordering of PS-*b*-P8FMA. The higher periodicity of LC structure could also be inferred from the sharper scattering peak attributed to 0.53 nm spacing, which corresponds to the distance between adjacent CF_3-end of semi-fluorinated side chain [41]. To determine the the two chacteristic orientations of the BCP microclyinder and LC mesogen, the shear-flow orientation in this side chain liquid crystalline PS-*b*-P8FMA was investiagted by SAXS measurements (Figure 4). From the obtained SAXS patterns with X-ray irradiated to three characteristic directions, vorticity ($v \times \nabla v$), velocity (v), and velocity gradient (∇v) directions, obviously the microcylinder is oriented normal to the LC smectic layer because of the indicated two distincitve preferential scattering singals with a near 90° intersection angle in vorticity ($v \times \nabla v$) and velocity gradient (∇v) directions. In the velocity (v) direction, the reflections are expected to appear as six characteristics spots if the microcylinders are preferentially oriented along the velocity direction [44]. However, because of the insufficent long-ranged orders possibly suffering from a low χN value ($\chi N = 16.9$), the expected characteristics sattering spots from the hexagonal packing array of microcylinders are not significant. Besides, different from the other two directions, no scattering signals from LC smectic layers were revealed because the irradiated X-ray beam is almost normal to the lying smectic layer strucuture. The two orientations of BCP domains and side chain LC mesogens perpendicular to each other were also reported in other SCLC BCP systems [45, 46].

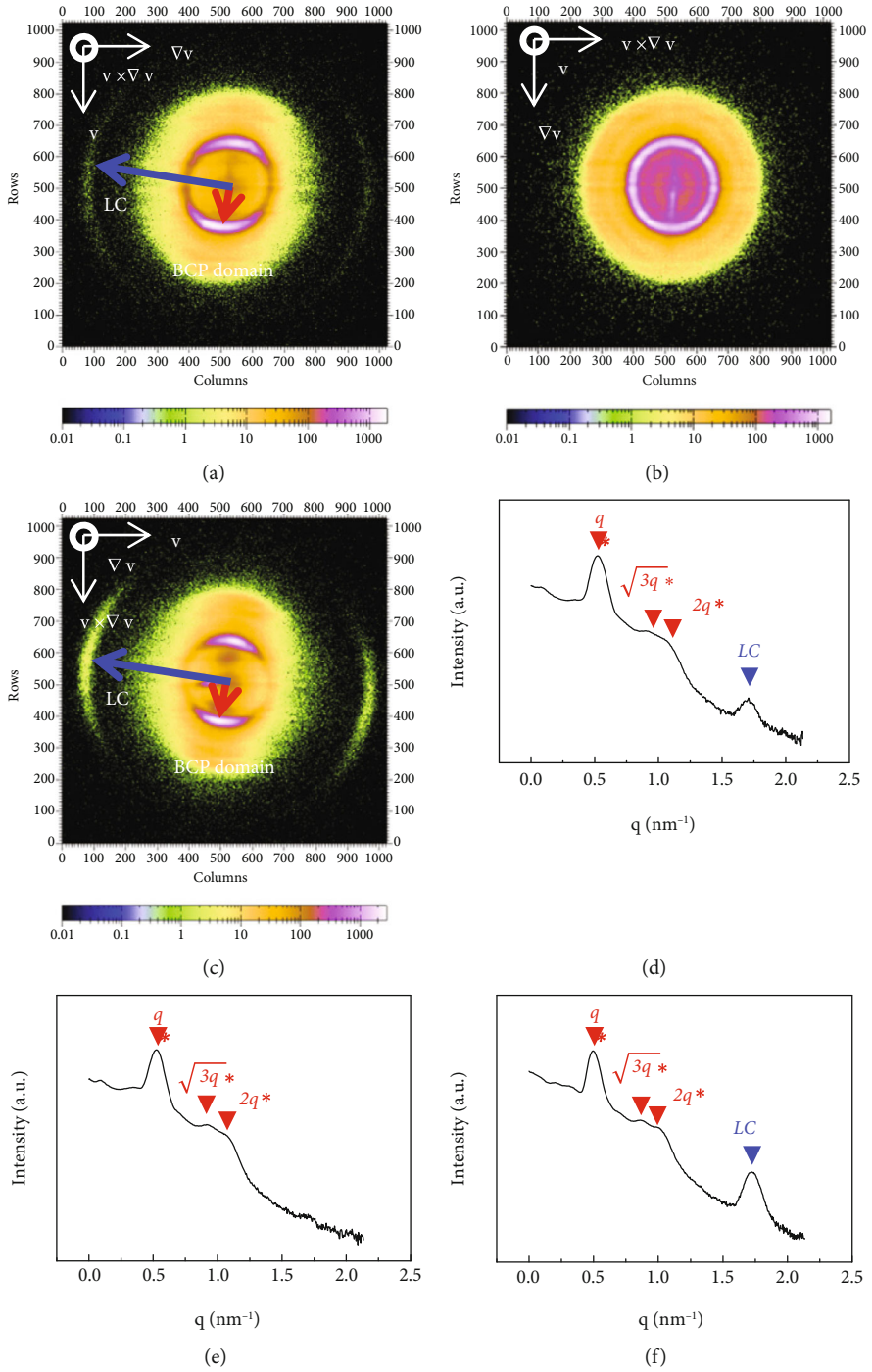

Figure 4: SAXS patterns of PS-*b*-P8FMA sheared in the isotropic phase at 200°C at rates of 5 s^{-1} and following thermal annealing at 150°C in the smectic phase for 3 h. The SAXS measurements were performed at room temperature by irradiating the X-ray beam along (a) vorticity ($v \times \nabla v$), (b) velocity (v), and (c) velocity gradient (∇v) directions. The observed patterns in indicate that the preferential orientation of BCP cylindrical domains is along the velocity direction and the smectic layers consisted of perfluoroalkyl side chains are arranged vertical to the BCP domains in the velocity direction. And the 1-D integration profile of 2-D SAXS pattern along the radius to the circle center by irradiating the X-ray beam along (d) vorticity ($v \times \nabla v$), (e) velocity (v), and (f) velocity gradient (∇v) directions. The smectic layer orientation is suggested by the absence of the smectic layer reflection in SAXS pattern irradiating X-ray beam from (b) the neutral velocity gradient direction. The scattering peaks attributed to hexagonally packed cylinderical BCP domain and LC side chain ordering are marked with red and navy triangle markers, respectively.

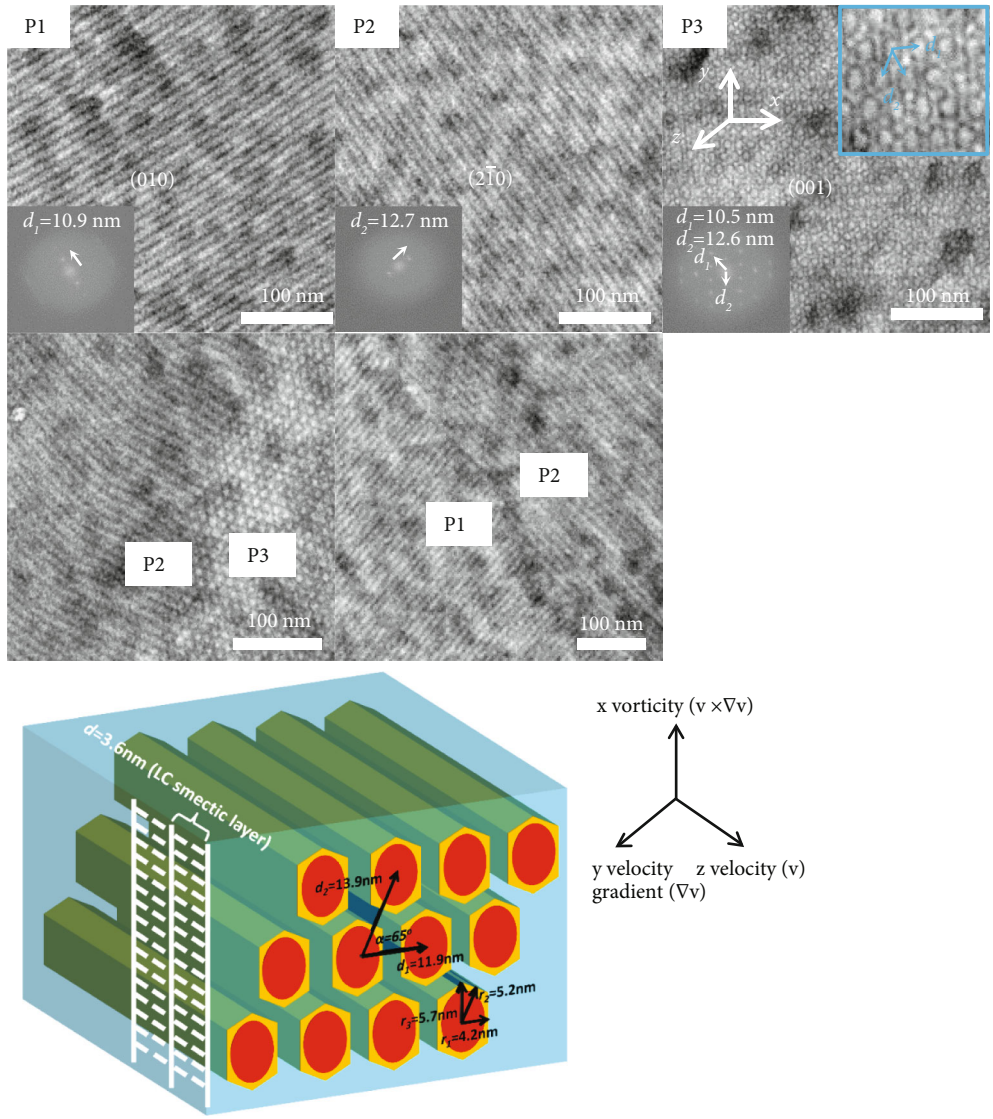

FIGURE 5: TEM micrographs showing the anisotropic hexagonally packed ellipsoids of the annealed PS-*b*-P8FMA bulk sample. Three phases noted as P1, P2, and P3 are in response to the striations of two distinctive dimensions from (010) and (2$\bar{1}$0) directions in side view and the anisotropic hexagonally packed array in top view.

Besides, the self-assembly structure resulting from block segregation was also revealed by X-ray analysis in combination with TEM. In SAXS characterizations, characteristic q ratios of $1:\sqrt{3}:2:\sqrt{7}:\sqrt{12}$ were observed and hexagonall packed cylinderical morhology was thereby assigned. However, in TEM characteization three distinctive phases could be observed: two striation phase with characterisitc 10.9 and 12.7 nm d_{spacing}, respectively, and a hexgonally packed array consisted of these two distinctive d_{spacing} (Figure 5). In addition, the grain boundaries between those distinctive phases were clearly revealed in TEM images. The inset of TEM image clearly reveals the hexgonally packed array of significant anisotropy in which the bright elliptical PS domains are surrounded by the segments attached with LC side chains. The observed middle dark interface was possibly caused by intensive accumulated ruthenium tetra-oxide stained on hydroxyl groups in the backbone of P8FMA segments, which is consistent with the proposed head-to-head configuration in side chain ordering. The bottom left inset in TEM images displays the Fourier-transform pattern of the real-space image. The array of anisotropic hexagonally packed cylinder in shear flow was further proposed based on X-ray and TEM results and the characteristic dimensions were noted as shown in the below scheme. Here, the core elliptical PS (red) and shell P8FMA backbone (orange) domains are approximated as an integrated PS hexagon because of negligible volume fraction of the P8FMA backbone. The simplified PS volume fraction calculated from the model ($f_{\text{PS}} = 0.46$) is consistent with that ($f_{\text{PS}} = 0.50$) estimated from M_{n} of block. In this model, the normal vector of (001) plane consisted of PS cylinder in hexagonally packing array is parallel to the velocity direction and LC director axis is along the velocity direction as well.

The fast Fourier transform of this anisotropic array was further given by Image-J (Figure S10(a), SI). Two distinctive $d_{spacing}$ with a 125° intersection angle and their secondary singals at $\sqrt{3}:2:\sqrt{7}$ $q$positions were successfully assgined. These sginals were further intergrated along the radius to the center and a 1-D integration profile was obtained (Figure S10(c), SI). The peak posititons in the integrated profile could be correlated with those in SAXS profile. And the overlapped signals from two distinctive $d_{spacing}$ possibly lead to the broader scattering peaks of PS-*b*-P8FMA compared to other studied BCPs. A schematic illustration on the hierarchical structure of PS-*b*-P8FMA is further proposed based on the X-ray and TEM characterization results. The orientation of PS microcylinder is aligned vertical to the 3.6-nm-width LC smectic layer consisted of a pair of perfluoroakyl side chain in head-to-head regularity. Because of the chain-stretching confinements brought by the LC side chain ordering, the surrounded PS domain may take the elliptical shape in order to minimize the free energy of the hierachcial self-assembly system.

To further investigate the interpaly between block segregation between LC ordering, SAXS was taken at temperatures higher than the observed T_{iso} of PS-*b*-P8FMA (Figure S11, SI). As the annealing temperature is cooling from 250°C to 190°C, the intensities of characteristic secondary peaks at $\sqrt{3}:2:\sqrt{7}$ q positions indicating the hexagonal packing arrray became increased, suggesting an ehanced hexgonally packing ordering. The observed hexongall packed cylinder morpholgy with thermaldyanmics stability was against the predicted laemllar morpholgy from self-assembly of symmrteic volume fraction using flexible coil–coil model [1]. The inconsistence was attibuted to the unneglectable rigidity difference from blocks of sigingicantly unequal statistical segments legnth [12, 47, 48], which is obviously caused by the incorporated perfluorinated side chain. As the temperature was further cooled to 170°C, the scattering peak attributed to LC side chain ordering at high q region began to appear, which is in good agreement with detected T_{iso} at 171.6°C in DSC analysis. The ordering of LC side chain was increased with elongated spacing with lowering temperature. Accordingly, the domain spacing determined by the position of primary scattering peak became smaller, which is against the change of χ parameter and unperturbed chain dimension (R_g), as the domain spacing will be increased by the higher χ parameter and larger R_g at lower temperature [49]. Besides, at lower temperature the relatively intensities of secondary peaks at $\sqrt{3}:2:\sqrt{7}$ q positions to the primary peak became basically constant, indicating a thermodynamics stable morphology from block segregation under T_{iso}. Therefore, a morphology transition from isotropic to anisotropic hexagonal packing array caused by the appearance of LC side chain ordering could be inferred.

3.4. Estimation of χ_{eff}. To quantify the strength of the segregation of PXFMA against PS, the random-phase approximation (RPA) method [40] was used, in which the effective Flory–Huggins interaction parameter is expressed by $\chi_{eff} = A/T + B$, where A/T is the enthalpic contribution, and B is the entropic contribution. First, temperature-dependent SAXS measurements were conducted on PS-*b*-PXFMA ($X = 4$, 6, or 8), starting in 10°C decrements (Figure S12, SI), which are all above ODTs of BCPs (Figure S13, SI). As all measuring temperatures are well-above the LC isotropic transition temperature of C_6F_{13} or C_8F_{17}-based side chains, no modification from side chain LC ordering is included into the existed RPA method based on flexible coil–coil model [49]. Herein, the SAXS profiles in the mean-field disordered state were then analyzed based on Leibler's mean-field theory, which is modified to include the effects from the dispersity and volume asymmetry of segments. Remarkably, as χ_{eff} is dependent on the reference volume used to calculate N, a common reference volume ($v_0 = 118$ Å^3) was used for the comparison between the estimated χ_{eff} and other reported values.

The χ_{eff} of S4F, S6F and S8F was expressed by $\chi_{eff\ PS/P4FMA} = 7.1/T + 0.139$, $\chi_{eff\ PS/P6FMA} = 8.2/T + 0.142$ and $\chi_{eff\ PS/P8FMA} = 21.5/T + 0.172$ (Tables S2—S4). $X_{eff}$of S1F was previously reported by our group with an expression of $\chi_{eff\ PS/P1FMA} = 19.4/T + 0.126$ [40]. The difference in the enthalpic contributors may come from the distinctive M_n and dispersities of BCPs of varied chain end effects. Considering the estimated χ_{eff} of BCPs with varied side chain lengths at 150°C annealing temperature ($\chi_{eff\ PS/P1FMA} = 0.172$, $\chi_{eff\ PS/P4FMA} = 0.155$, $\chi_{effPS/P6FMA} = 0.161$ and $\chi_{eff\ PS/P8FMA} = 0.223$), the driving forces of block segregation are further quantified based on the known M_n of BCPs ($\chi_{eff\ PS/P1FMAN} = 10.5$, $\chi_{eff\ PS/P4FMAN} = 11.3$, $\chi_{eff\ PS/P6FMAN} = 11.2$ and $\chi_{eff\ PS/P8FMAN} = 16.9$). The estimated driving forces are of the similar magnitudes, however, in bulk study a morphology transition of BCPs with increased side chain lengths was clearly observed. Therefore, the significant differences on morphologies are reasonably correlated to the LC ordering of introduced side chain.

Besides, all estimated χ_{eff} of BCPs with semi-fluorinated side chains are several times higher than that of commonly used poly(styrene-*b*-methyl methacrylate) (PS-*b*-PMMA). For instance, χ_{eff} value of PS-*b*-PMMA at 25°C was measured being 0.04 [50], which was barely 1/6 of $\chi_{eff\ PS/P8FMA} = 0.244$ at 25°C. The measured higher χ_{eff} is also indicated by the significantly unbalanced SFEs of counter-blocks in contact-angle characterization.

3.5. Domain Orientation Control in Thin Film. Owing to the potential for creating a variety of morphologies in thin film, PS-*b*-P8FMA was spin-coated onto BSLs of distinctive SFEs. In this study, two synthesized random copolymers poly-(methyl methacrylate-*random*-2,2,2-trifluoroethyl methacrylate-*random*-methacrylic acid) (PMMA-*r*-PTFEMA-*r*-PMAA) (Figure S14 and Table S5, SI) of various compositions were spin-coated onto bare silicon substrate and cross-linked to induce the desired orientation of BCP on top bottom substrate. In all used BSL copolymers, approximately 3% weight fraction of methacrylic acid was added as cross-linking functionalities. PTFEMA and PMMA units were selected for tuning SFE of BSL, because SFE of PTFEMA and PMMA is found close to SFE of P8FMA and PS block, respectively (Table S6, SI). The periodic length of thin film pattern obtained from AFM

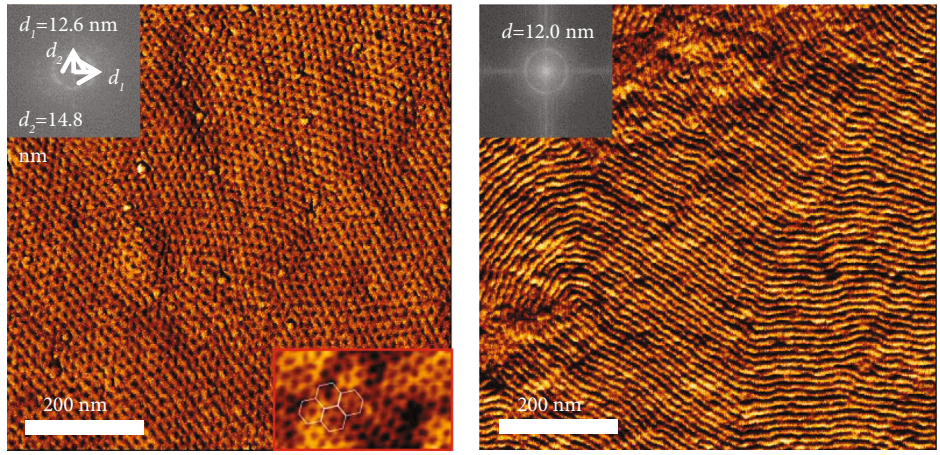

(a) (b)

Figure 6: AFM phase images of the thin films prepared from PS-*b*-P8FMA on various BSLs: (a) (43-54-3) and (b) (77-20-3). The BCP thickness is controlled being 1.5 L_0. The upper left inset displays the Fourier-transform pattern of the real-space image and the periodic length of domain is estimated from FFT. The inset of AFM height image in (a) shows the hexagonally packing array over the magnified scanning area.

characterizations was extracted from fast Fourier transform (FFT).

The AFM phase images (Figure 6) reveal the morphologies of PS-*b*-P8FMA on BSLs of distinctive SFEs. A neutral BSL (43-54-3) without any preferential interaction to the either block was first obtained. Therefore, the BCP domains perpendicular to the substrate was achieved. As shown in the inset image, a hexagonally packed array perpendicular to the substrate was observed. Two distinctive $d_{spacing}$ of 12.6 nm and 14.8 nm obtained from FFT characterized in thin film was highly consistent with the spacing observed in bulk state. Remarkably, following the selective etching of surrounding P8FMA-based segments, a clearer hexagonally packing array of PS cylinders with significant anisotropy was revealed by AFM characterization (Figure S15, SI).

As the composition of PTFEMA in BSL was reduced, the ontop PS-*b*-P8FMA begins to exhibit a morphology transition from perpendicular hexagonally packed cylinders to long-ranged striation patterns of 12.0 nm domain spacing with half-pitch of 6.0 nm. The striation pattern was thought in response to the parallel oriented PS cylinder domain on the substrate, as the used BSL (77-20-3) is slightly preferential to PS segments. Conclusively, the precise adjustments on aligned orientation of PS domain enable the facile tailoring on thin film pattern type.

4. Conclusion

In this study, semi-fluorinated C_8F_{17}-containing LC side chain was introduced to the backbone of precursor BCP PS-*b*-PGMA for enhanced segregation and precise thin film orientation control, which enables the facile tailoring on pattern type without any additional efforts. The observed hexagonally packed cylindrical morphology of PS-*b*-P8FMA exhibits anisotropic characteristics with smectic side chain ordering. As the length of side chain is gradually reduced to $-C_6F_{13}$, $-C_4F_9$, and $-CF_3$, a gradual phase transition from smectic to amorphous state is revealed. Accordingly, an isotropic hexagonally packed cylinder or lamellae-based morphology is observed for symmetric BCPs, indicating the increased influences from enhanced side chain ordering on the self-assembled morphology. Besides, a hierarchical self-assembly structure model including both block segregation and LC ordering characteristic spacing is proposed. The domain orientation of PS-*b*-P8FMA in thin film is readily adjusted by varying the composition of copolymers as BSL. The long-range ordered striations and hexagonally packed dots pattern, in response to parallel and vertical domain orientation, respectively, are thereby prepared by simply tuning the compositions of BSLs without changing BCPs or application of additional techniques. Therefore, the fine orientation control on BCP domains could be successfully achieved, in response to the specific chemically modified bottom surface region. This simple but high efficiency approach to tailoring BCP pattern type enables the easy fabrication of various sub-10 nm half-pitch patterns in lithographic application.

Conflicts of Interest

The authors declare no competing financial interest.

Acknowledgments

The authors thank Prof. Tomoyasu Hirai of Department of Applied Chemistry, Osaka Institute of Technology for kindly assisting with synchrotron SAXS experiments. The synchrotron radiation experiments were performed at BL40B2 of SPring-8 with the approval of the Japan Synchrotron Radiation Research Institute (JASRI) (Proposal no. 2019A1173). The authors thank Prof. Masatoshi Tokita of Department of Chemical Science and Engineering, Tokyo Institute of Technology for kindly assisting with steady shear alignments. The author Lei Dong acknowledges the financial support of 2021 Jiangsu Province Shuangchuang (Innovation and Entrepreneurship)

Talent Program (No. JSSCBS20210067) and State Key Laboratory of High Performance Civil Engineering Materials Open Fund (No. 2021CEM002).

Supplementary Materials

Figure S1. ^{1}H NMR spectra of 1,1,1,2,2,3,3,4,4-nonafluoro-6-iodohexane (black) in acetone-d_6 and the synthesized 3,3,4,4,5,5,6,6,6-nonafluoro-1-hexanethiol (red) in chloroform-*d*. Table S1. Characteristics of the synthesized homopolymers. Figure S2. ^{1}H NMR spectra of synthesized homo-PGMA and post-functionalized homo-PXFMA ($X = 4, 6$ and 8) in $CDCl_3$ solvent. The below right number indicates the molecular weight of each homopolymer. Figure S3. SEC chromatograms of the precursor homo-PGMA and post-functionalized homo-PXFMA ($X = 4, 6$ and 8) in THF eluent. The below right number indicates the molecular weight of each homopolymer. Figure S4. DSC curves of the synthesized homo-PXFMA ($X = 4, 6$ and 8) at (a) a heating and a cooling rate of 10°C/min under nitrogen atmosphere, respectively. Figure S5. WAXD profiles of the homo-PXFMA ($X = 4, 6$ or 8) following thermal annealing. Figure S6. The optimized conformations of model compounds with various side chains using MM2 energy-minimization based on Chem 3D 16.0. The below right scheme represents the LC lamellar structure consisted of a pair of mesogens with end-to-end stereo-regularity. Figure S7. SEC chromatography of precursor PS-*b*-PGMA (SG4) and corresponding PS-*b*-PXFMA (SXF, $X = 1, 4, 6$ and 8) after post functionalization. Figure S8. DSC curves of the studied PS-*b*-PXFMA (SXF, $X = 1, 4, 6$ and 8) at a heating rate of 10°C/min under nitrogen atmosphere in heating and cooling cycles. The noted transition temperatures are estimated from the heating cycles. Figure S9. The experimental SAXS profile (black scatters) and the fitted SAXS profiles (red line) based on the model shown in the insets of (a) PS-*b*-P1FMA, (b) PS-*b*-P4FMA and (c) PS-*b*-P6FMA using Scatter (Version 2.5, 03/2011) 1D (scatter curve). The insert figure in (c) shows the hexagonally packed cylinder in top (left) and side (right) views and the red scales in nanometer units are also given in each inset. Figure S10. (a) The fast Fourier transform of P3 phase and the signals in response to d_1 and d_2, as labeled in blue and red circle, respectively. The green circle indicates the overlapping signals from $\sqrt{3}q$ of d_1 and $2q$ of d_2. (b) The TEM images showing the dimension a_1 and a_2 in response to d_1 and d_2, respectively, in anisotropic hexagonal packing array. (c) The 1-D integration profile of (a) along the radius to the center of image and the signals from two spacings were labeled. (d) The experimental SAXS 1-D integration profile in comparison with (c). Figure S11. SAXS profiles of PS-*b*-P8FMA bulk sample taken at varied temperatures in a cooling process. The blue triangle marker indicates the scattering peak from LC side chain ordering. The estimated domain spacing of self-assembly morphology becomes smaller with reduced temperatures. Figure S12. The scattering profiles (dotted lines) measured by SAXS and the fitting profiles (smooth lines) at different temperatures for (a) PS-*b*-P4FMA (S4F), (b) PS-*b*-P6FMA (S6F) and (c) PS-*b*-P8FMA (S8F). Figure S13. Temperature dependences of the effective Flory–Huggins interaction parameter for (a) PS-*b*-P4FMA (S4F), (b) PS-*b*-P6FMA (S6F) and (c) PS-*b*-P8FMA (S8F) using a reference volume of 118 Å^3. Table S2. The fixed parameters used to estimate χ_{eff} for PS-*b*-PXFMA. ($X = 4, 6$ or 8). Table S3. The estimated parameters χ_{eff} for PS-*b*-PXFMA at varied temperatures. ($X = 4, 6$ or 8). Table S4. Estimated enthalpic and entropic contributions for PS-*b*-PXFMA. ($X = 4, 6$ or 8). Figure S14. (a) ^{1}H NMR spectra and (b) GPC chromatograms of the synthesized random copolymers PMMA-*r*-PTFEMA-*r*-PMAAs. The labeled number in XX–YY–ZZ form indicates the weight fraction of three comonomers MMA, TFEMA and MAA in percentage. Table S5. Characteristics of the synthesized BSL copolymers. Table S6. Contact angles and surface free energies (SFEs) of homopolymers. Figure S15. The AFM phase image of the thin film prepared from PS-*b*-P8FMA on BSL (43-54-3) following oxygen plasma etching. The inset reveals the fast Fourier transform of the image and the signals in response to d_1 and d_2 are marked. The inset magnified AFM images shows the dimension a_1 (blue marker) and a_2 (red marker) in response to d_1 and d_2, respectively, in anisotropic hexagonal packing array. *(Supplementary Materials)*

References

[1] L. Leibler, "Theory of microphase separation in block copolymers," *Macromolecules*, vol. 13, no. 6, pp. 1602–1617, 1980.

[2] F. S. Bates and G. H. Fredrickson, "Block copolymer thermodynamics—theory and experiment," *Annual Review of Physical Chemistry*, vol. 41, no. 1, pp. 525–557, 1990.

[3] F. S. Bates and G. H. Fredrickson, "Block copolymers—designer soft materials," *Physics Today*, vol. 52, no. 2, pp. 32–38, 1999.

[4] S. Kurimoto, L. Tong, H. Maeda, Y. Nabae, and T. Hayakawa, "Long-range ordered double Gyroid structures via solution casting from poly(2,2,2-trifluoroethyl methacrylate)-block-poly(2-vinyl pyridine)," *Macromolecular Chemistry and Physics*, vol. 222, no. 22, p. 2100272, 2021.

[5] W. C. Liu, L. B. Zhang, R. Chen, X. Wu, S. Yang, and Y. Y. Wei, "The phase aggregation behavior of the blend materials block copolymer polystyrene-b-polycarbonate (PS-b-PC) and homopolymer polystyrene (PS)," *Macromolecular Chemistry and Physics*, vol. 222, no. 8, p. 2000432, 2021.

[6] C. J. Hawker and T. P. Russell, "Block copolymer lithography: merging "bottom-up" with "top-down" processes," *MRS Bulletin*, vol. 30, no. 12, pp. 952–966, 2005.

[7] M. Ohke and J. Matsui, "Rapid formation of a lamellar structure in an amphiphilic comb-shaped polymer by nanophase separation using microwave-humidity annealing," *Macromolecular Chemistry and Physics*, vol. 223, no. 3, p. 2270005, 2022.

[8] K. Watanabe, S. Katsuhara, H. Mamiya et al., "Downsizing feature of microphase-separated structures via intramolecular crosslinking of block copolymers," *Chemical Science*, vol. 10, no. 11, pp. 3330–3339, 2019.

[9] J. E. Poelma, K. Ono, D. Miyajima, T. Aida, K. Satoh, and C. J. Hawker, "Cyclic block copolymers for controlling feature sizes in block copolymer lithography," *ACS Nano*, vol. 6, no. 12, pp. 10845–10854, 2012.

[10] Y. Asai, K. Yamada, M. Yamada, A. Takano, and Y. Matsushita, "Formation of tetragonally-packed rectangular

cylinders from ABC block terpolymer blends," *ACS Macro Letters*, vol. 3, no. 2, pp. 166–169, 2014.

[11] J. Y. Yu, F. Q. Liu, P. Tang, F. Qiu, H. D. Zhang, and Y. L. Yang, "Effect of geometrical asymmetry on the phase behavior of rod-coil Diblock copolymers," *Polymers*, vol. 8, no. 5, p. 184, 2016.

[12] V. Pryamitsyn and V. Ganesan, "Self-assembly of rod–coil block copolymers," *The Journal of Chemical Physics*, vol. 120, no. 12, pp. 5824–5838, 2004.

[13] J. Gao, P. Tang, and Y. L. Yang, "Non-lamellae structures of coil-semiflexible diblock copolymers," *Soft Matter*, vol. 9, no. 1, pp. 69–81, 2013.

[14] N. A. Kumar and V. Ganesan, "Communication: self-assembly of semiflexible-flexible block copolymers," *Journal of Chemical Physics*, vol. 136, no. 10, article 101101, 2012.

[15] Y. Zhao, B. Qi, X. Tong, and Y. Zhao, "Synthesis of double side-chain liquid crystalline block copolymers using RAFT polymerization and the orientational cooperative effect," *Macromolecules*, vol. 41, no. 11, pp. 3823–3831, 2008.

[16] S. Nagano, "Random planar orientation in liquid-crystalline block copolymers with azobenzene side chains by surface segregation," *Langmuir*, vol. 35, no. 17, pp. 5673–5683, 2019.

[17] X.-Q. Jiang, R.-Y. Zhao, W.-Y. Chang et al., "Highly ordered sub-10 nm patterns based on multichain columns of side-chain liquid crystalline polymers," *Macromolecules*, vol. 52, no. 13, pp. 5033–5041, 2019.

[18] E. Verploegen, T. Zhang, N. Murlo, and P. T. Hammond, "Influence of variations in liquid-crystalline content upon the self-assembly behavior of siloxane-based block copolymers," *Soft Matter*, vol. 4, no. 6, pp. 1279–1287, 2008.

[19] S. W. Cheng, Y. Hu, X. H. Wu, W. Li, and J. S. Mu, "Hierarchical self-assembly of polyethylene midblock copolymers in hot steam: key role of crystalline and topological structure," *Macromolecular Chemistry and Physics*, vol. 222, no. 7, p. 2000419, 2021.

[20] M. Shah, V. Pryarnitsyn, and V. Ganesan, "A model for self-assembly in side chain liquid crystalline block copolymers," *Macromolecules*, vol. 41, no. 1, pp. 218–229, 2008.

[21] X. K. Li, F. Huang, T. Jiang, X. H. He, S. L. Lin, and J. P. Lin, "Phase behaviors of side chain liquid crystalline block copolymers," *RSC Advances*, vol. 5, no. 2, pp. 1514–1521, 2015.

[22] Y. S. Lv, L. Q. Wang, F. S. Wu, S. T. Gong, J. Wei, and S. L. Lin, "Self-assembly and stimuli-responsive behaviours of side-chain liquid crystalline copolymers: a dissipative particle dynamics simulation approach," *Physical Chemistry Chemical Physics*, vol. 21, no. 14, pp. 7645–7653, 2019.

[23] B. Sun, Z. W. Xu, Z. M. Tang, C. H. Cai, and J. P. Lin, "Dot nanopattern self-assembled from rod-coil block copolymer on substrate," *Macromolecular Chemistry and Physics*, vol. 221, no. 18, p. 2000254, 2020.

[24] L.-Y. Shi, J. Lan, S. Lee, L.-C. Cheng, K. G. Yager, and C. A. Ross, "Vertical lamellae formed by two-step annealing of a rod–coil liquid crystalline block copolymer thin film," *ACS Nano*, vol. 14, no. 4, pp. 4289–4297, 2020.

[25] L.-Y. Shi, S. Lee, L.-C. Cheng et al., "Thin film self-assembly of a silicon-containing rod–coil liquid crystalline block copolymer," *Macromolecules*, vol. 52, no. 2, pp. 679–689, 2019.

[26] I. W. Hamley, V. Castelletto, Z. B. Lu, C. T. Imrie, T. Itoh, and M. Al-Hussein, "Interplay between smectic ordering and microphase separation in a series of side-group liquid-crystal block copolymers," *Macromolecules*, vol. 37, no. 13, pp. 4798–4807, 2004.

[27] T. Qu, S. Guan, X. Zheng, and A. Chen, "Perpendicularly aligned nanodomains on versatile substrates via rapid thermal annealing assisted by liquid crystalline ordering in block copolymer films," *Nanoscale Advances*, vol. 2, no. 4, pp. 1523–1530, 2020.

[28] F. Liao, L.-Y. Shi, L.-C. Cheng et al., "Self-assembly of a silicon-containing side-chain liquid crystalline block copolymer in bulk and in thin films: kinetic pathway of a cylinder to sphere transition," *Nanoscale*, vol. 11, no. 1, pp. 285–293, 2019.

[29] K. Nickmans, J. N. Murphy, B. de Waal et al., "Sub-5 nm patterning by directed self-assembly of oligo (dimethylsiloxane) liquid crystal thin films," *Advanced Materials*, vol. 28, no. 45, pp. 10068–10072, 2016.

[30] M. Al-Hussein, Y. Serero, O. Konovalov, A. Mourran, M. Moller, and W. H. de Jeu, "Nanoordering of fluorinated side-chain liquid crystalline/amorphous diblock copolymers," *Macromolecules*, vol. 38, no. 23, pp. 9610–9616, 2005.

[31] T. Y. Lo, A. Dehghan, P. Georgopanos, A. Avgeropoulos, A. C. Shi, and R. M. Ho, "Orienting block copolymer thin films via entropy," *Macromolecules*, vol. 49, no. 2, pp. 624–633, 2016.

[32] E. Verploegen, T. Zhang, Y. S. Jung, C. Ross, and P. T. Hammond, "Controlling the morphology of side chain liquid crystalline block copolymer thin films through variations in liquid crystalline content," *Nano Letters*, vol. 8, no. 10, pp. 3434–3440, 2008.

[33] H. L. Xie, X. Li, J. Ren, C. Bishop, C. G. Arges, and P. F. Nealey, "Controlling domain orientation of liquid crystalline block copolymer in thin films through tuning mesogenic chemical structures," *Journal of Polymer Science Part B: Polymer Physics*, vol. 55, no. 6, pp. 532–541, 2017.

[34] M. Komura, A. Yoshitake, H. Komiyama, and T. Iyoda, "Control of air-Interface-induced perpendicular nanocylinder orientation in liquid crystal block copolymer films by a surface-covering method," *Macromolecules*, vol. 48, no. 3, pp. 672–678, 2015.

[35] K. Fukuhara, Y. Fujii, Y. Nagashima, M. Hara, S. Nagano, and T. Seki, "Liquid-crystalline polymer and block copolymer domain alignment controlled by free-surface segregation," *Angewandte Chemie International Edition*, vol. 52, no. 23, pp. 5988–5991, 2013.

[36] T. J. Wang, X. Li, Z. J. Dong, S. Huang, and H. F. Yu, "Vertical orientation of nanocylinders in liquid-crystalline block copolymers directed by light," *ACS Applied Materials & Interfaces*, vol. 9, no. 29, pp. 24864–24872, 2017.

[37] T. Isono, B. J. Ree, K. Tajima, R. Borsali, and T. Satoh, "Highly ordered cylinder morphologies with 10 nm scale periodicity in biomass-based block copolymers," *Macromolecules*, vol. 51, no. 2, pp. 428–437, 2018.

[38] S. Y. Dieng, B. Bertaina, and A. Cambon, "Synthese et application de nouveaux sulfures a chaine perfluoree," *Journal of Fluorine Chemistry*, vol. 28, no. 3, pp. 341–355, 1985.

[39] L. Leemans, R. Fayt, P. Teyssié, H. Uytterhoeven, and W. De Winter, "Controlled "Living" anionic polymerization of glycidyl methacrylate," *Journal of Polymer Science Part A: Polymer Chemistry*, vol. 28, no. 8, pp. 2187–2193, 1990.

[40] Y. Yoshimura, A. Chandra, Y. Nabae, and T. Hayakawa, "Chemically tailored high-χ block copolymers for perpendicular lamellae via thermal annealing," *Soft Matter*, vol. 15, no. 17, pp. 3497–3506, 2019.

[41] J. G. Wang, G. P. Mao, C. K. Ober, and E. J. Kramer, "Liquid crystalline, semifluorinated side group block copolymers with stable low energy surfaces: synthesis, liquid crystalline structure, and critical surface tension," *Macromolecules*, vol. 30, no. 7, pp. 1906–1914, 1997.

[42] L. Dong, A. Chandra, K. Wylie, R. Nakatani, Y. Nabae, and T. Hayakawa, "The role of liquid crystalline side chains for long-range ordering in the block copolymer thin films," *Journal of Photopolymer Science and Technology*, vol. 33, no. 5, pp. 529–536, 2020.

[43] M. Harris, G. Appel, and H. Ade, "Surface morphology of annealed polystyrene and poly(methyl methacrylate) thin film blends and bilayers," *Macromolecules*, vol. 36, no. 9, pp. 3307–3314, 2003.

[44] M. Tokita, M.-A. Adachi, S. Masuyama, F. Takazawa, and J. Watanabe, "Characteristic shear-flow orientation in LC block copolymer resulting from compromise between orientations of microcylinder and LC mesogen," *Macromolecules*, vol. 40, no. 20, pp. 7276–7282, 2007.

[45] E. Verploegen, L. C. McAfee, L. Tian, D. Verploegen, and P. T. Hammond, "Observation of transverse cylinder morphology in side chain liquid crystalline block copolymers," *Macromolecules*, vol. 40, no. 4, pp. 777–780, 2007.

[46] M. Koga, K. Sato, S. Kang, and M. Tokita, "Microphase-separated morphology and liquid crystal orientation in block copolymers comprising a main-chain liquid crystalline central segment connected to side-chain liquid crystalline segments at both ends," *Macromolecular Chemistry and Physics*, vol. 219, no. 3, p. 1700332, 2018.

[47] F. S. Bates, M. F. Schulz, A. K. Khandpur et al., "Fluctuations, conformational asymmetry and block copolymer phase behaviour," *Faraday Discussions*, vol. 98, pp. 7–18, 1994.

[48] C.-C. Ho, Y.-H. Lee, C.-A. Dai, R. A. Segalman, and W.-F. Su, "Synthesis and self-assembly of poly(diethylhexyloxy-*p*-phenylenevinylene)-b-poly(methyl methacrylate) rod–coil block copolymers," *Macromolecules*, vol. 42, no. 12, pp. 4208–4219, 2009.

[49] N. Sakamoto and T. Hashimoto, "Order-disorder transition of low molecular weight polystyrene-block-polyisoprene. 1. SAXS analysis of two characteristic temperatures," *Macromolecules*, vol. 28, no. 20, pp. 6825–6834, 1995.

[50] T. P. Russell, R. P. Hjelm, and P. A. Seeger, "Temperature-dependence of the interaction parameter of polystyrene and poly(methyl methacrylate)," *Macromolecules*, vol. 23, no. 3, pp. 890–893, 1990.